Materials & Design 237 (2024) 112538

Contents lists available at ScienceDirect

Materials & Design

journal homepage: www.elsevier.com/locate/matdes

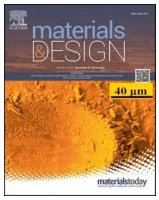

The columnar to equiaxed transition of CoCrNi medium-entropy alloy fabricated by laser directed energy deposition

Wenjie Zhao [a], Yonggang Sun [a], Pengcheng Che [a], Zhiliang Ning [a,*], Hongbo Fan [b], Haiyan Yang [c], Jianfei Sun [a], Peter K. Liaw [d], Alfonso H.W. Ngan [e,*], Yongjiang Huang [a,*]

[a] National Key Laboratory for Precision Hot Processing of Metals, Harbin Institute of Technology, Harbin 150001, China
[b] Space Environment Simulation Research Infrastructure, Harbin Institute of Technology, Harbin 150001, China
[c] Bazhou No.1 High School, Bazhou 065700, China
[d] Department of Materials Science and Engineering, University of Tennessee, Knoxville, USA
[e] Department of Mechanical Engineering, The University of Hong Kong, Pokfulam Road, Hong Kong, China

ARTICLE INFO

Keywords:
Laser directed energy deposition
CoCrNi medium-entropy alloy
Laser energy density
Columnar to equiaxed transition
Numerical simulation
Constitutional undercooling

ABSTRACT

Understanding and revealing the evolution mechanism of the columnar to equiaxed transition (CET) that occurred in the medium-entropy alloys (MEAs) fabricated by laser directed energy deposition (LDED) is crucial for achieving the tunable microstructure and mechanical properties. In the present work, a CET map was established to explain the effect of the laser energy density (LED) on the CET of the LDED fabricated single tracks of the CoCrNi MEA. The results show that the CET observed in single tracks is related to the morphological transformation of cellular substructure, which is governed by constitutional undercooling. With the increase of LED, the maximum value of the constitutional undercooling exceeds the critical nucleation undercooling earlier, which facilitates the heterogeneous nucleation and inhibits the epitaxial growth of rod-like cells, and finally causes a promoted CET. The correlation among the average cell size, geometrically necessary dislocation density, and average hardness of single tracks was also discussed. The present work not only uncovers the mechanism of the CET and grain growth in the LDED-fabricated CoCrNi MEA but also provides theoretical guidance for fabricating other MEAs with ideal microstructure and performance.

1. Introduction

High-entropy alloys (HEAs) and medium-entropy alloys (MEAs), also termed as multi-principal-element alloys (MPEAs) in an equimolar or near-equimolar ratio, have triggered considerable interest due to their excellent strength-ductility synergy, damage-tolerance, and fracture toughness [1–3]. Among major families of MPEAs, the face-centered cubic (FCC) ternary CoCrNi MEA exhibits higher strength and ductility as compared with those of the quaternary and quinary systems, especially at cryogenic temperatures [4,5]. In many studies, the CoCrNi MEA is fabricated by casting first and the subsequent deformation processes, such as rolling, forging, and high-pressure torsion [6,7]. In some cases, the annealing treatment is also required to obtain recrystallization or partial recrystallization microstructures [8,9]. Although these procedures enable the CoCrNi MEA to exhibit a superior combination of high strength and great ductility, they also have obvious limitations, such as low production efficiency and complex procedures. Hence, novel methodologies with the advantage of being efficient and convenient are urgent to be employed to fabricate the CoCrNi MEA with high performance.

Laser directed energy deposition (LDED) is a kind of additive manufacturing (AM) techniques that fabricates parts in a way of layer by layer, and has already attracted great attention due to its enviable advantage of being time-efficient and cost-effective as compared with conventional processes, especially for fabricating complex components [10–12]. The LDED process has been widely utilized to fabricate pure metals [13], Al-based alloys [14], Fe-based alloys (steels) [15], Ni-based alloys [16,52], and Ti-based alloys [17,51] with non-segregation, dense microstructures, and excellent mechanical properties. Recently, the LDED process has also been conducted to fabricate the CoCrNi MEA with excellent mechanical properties [18,19]. However, most of the research focuses on improving the performance of the LDED-fabricated CoCrNi MEA alloy, and there is a lack of literatures, which work on the solidification mechanism of the alloy. Xue et al. [20] reported that the

* Corresponding authors.
E-mail addresses: zhiliangning@sina.com (Z. Ning), hwngan@hku.hk (A.H.W. Ngan), yjhuang@hit.edu.cn (Y. Huang).

https://doi.org/10.1016/j.matdes.2023.112538
Received 13 March 2023; Received in revised form 13 November 2023; Accepted 3 December 2023
Available online 4 December 2023

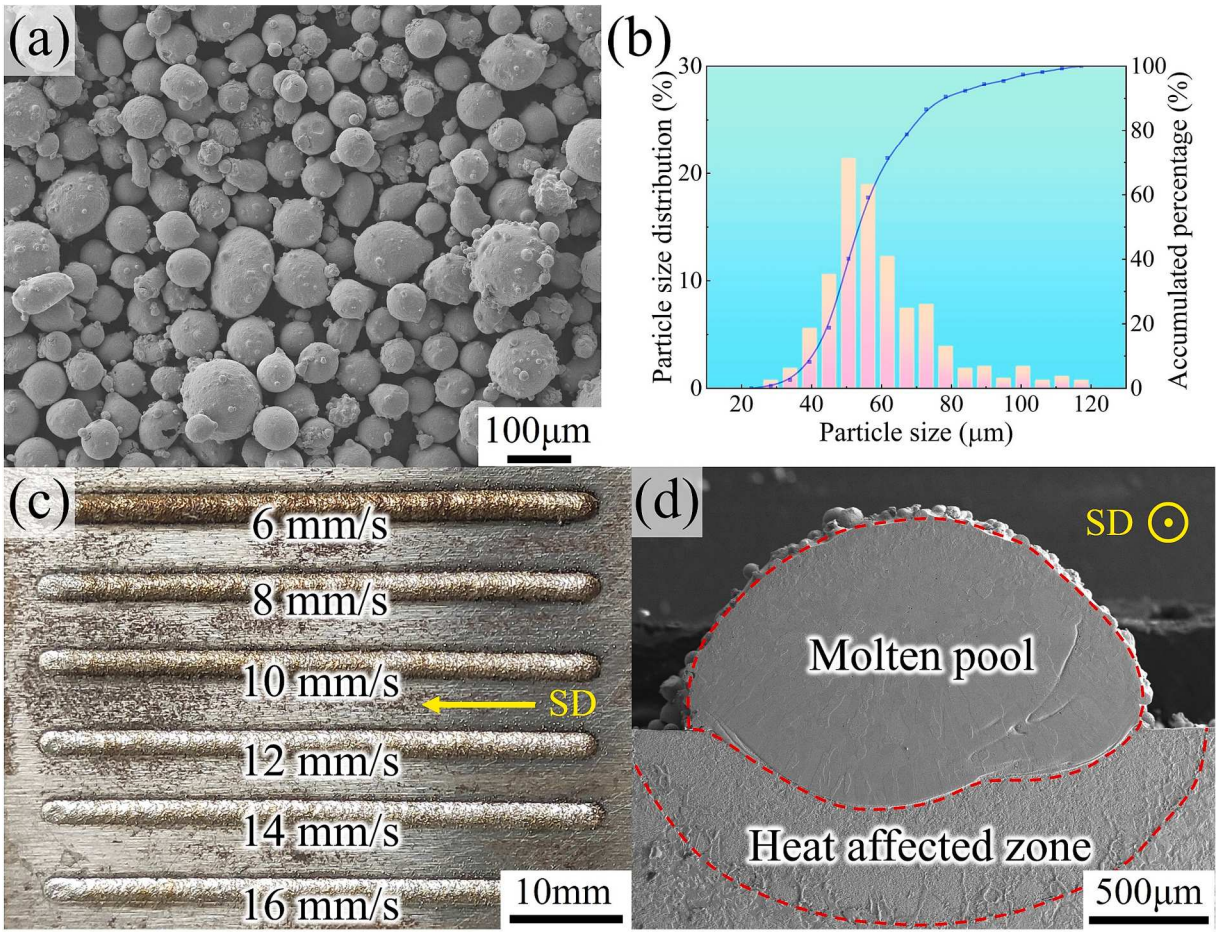

Fig. 1. (a) CoCrNi MEA powders used in the present work. (b) Powder size distribution. (c) LDED-fabricated single tracks. (d) The typical cross-sectional morphology of single track formed by laser power of 1000 W and scanning speed of 6 mm/s. SD means scanning direction.

mechanical properties of the LDED-fabricated CoCrNi MEA are largely dependent on the LDED parameters. In general, the solidification microstructure of LDED-fabricated CoCrNi MEA is mainly composed of columnar and equiaxed microstructures [21]. The columnar microstructure gives rise to directional properties whereas the equiaxed microstructure can result in isotropic properties. Therefore, revealing the correlation between LDED parameters and solidification microstructures is of essence for obtaining the desired microstructure and performance of the LDED-fabricated CoCrNi MEA.

Additionally, a morphological transition between these two types of solidification microstructures can also be observed in the LDED-fabricated CoCrNi MEA alloys, which is called the columnar-to-equiaxed transition (CET). According to the analytical model for CET developed by Hunt et al. [22], the proportion of the columnar microstructure and equiaxed microstructure in the solidification structure can be finely controlled by tuning solidification parameters, further determining the mechanical properties of the alloy. At present, systematic investigations based on Hunt's analytical model have been successfully employed to understand the mechanism of microstructure evolution in these kinds of metallic materials, but there is still the lack of the fundamental understanding of the grain growth and CET in the LDED-fabricated CoCrNi MEA, which severely restricts subsequently industrial productions and applications.

In the present work, the LDED technique was utilized to fabricate the single tracks of the CoCrNi MEA. Through experiment-simulation coupling, the evolution mechanism of the CET and the correlation between microstructure and hardness of the CoCrNi MEA single tracks were elucidated by establishing the relationship between LDED parameters, solidification conditions, and solidification microstructures. The present work will promote the further understanding of CET and grain-growth mechanisms of the LDED-fabricated CoCrNi MEA, and thus, lay a theoretical foundation for fabricating MEAs with desired microstructures and performance.

Table 1
LDED parameters used for fabricating CoCrNi MEA samples.

Parameters	Value
Laser power (W)	1000
Scanning speed (mm/s)	6, 8, 10, 12, 14, and 16
Laser beam spot diameter (mm)	2
Powder feed rate (g/min)	6
Protective gas flow rate (L/min)	5
Forming environment	Atmospheric condition

2. Experiments

2.1. Materials preparation and LDED process

The CoCrNi MEA powders used in the present work were fabricated by a gas-atomization technique (Beijing Yanbang New Material Technology Co., Ltd, China). Fig. 1 shows the SEM image and size distribution of the gas-atomized powders. The powder particles have spherical shapes (Fig. 1a), and the D50 value of the used powders is 53.5 μm (Fig. 1b). For the LDED process, a 45# steel of a 50 × 50 × 15 mm^3 dimension was chosen as the substrate. Before the deposition, the working surface of the substrate was carefully polished with a sandpaper

Table 2
Materials properties of the 45# steel [26] and CoCrNi MEA (calculated by JMatPro@).

Properties	45# steel	CoCrNi MEA
Density (kg/m^3)	7840	8270
Latent heat (J/kg)	2.47×10^5	3.06×10^5
Solidus temperature (K)	1623	1665
Liquidus temperature (K)	1773	1680

Table 3
Thermal physical properties of the 45# steel [26] and CoCrNi MEA (calculated by JMatPro@).

Temperature (K)	Thermal Conductivity (W·m^{-1}·K^{-1})		Heat Capacity (J·kg^{-1}·K^{-1})	
	45# steel	CoCrNi MEA	45# steel	CoCrNi MEA
298	47.15	11.33	472	440.89
473	45.25	14.56	480	470.06
673	38.23	18.26	524	502.2
873	37.07	21.95	615	535.71
1273	54.36	29.34	806	613.89

and cleaned in ethanol.

The single tracks of the CoCrNi MEA were fabricated on an LDED machine equipped with a 4000 W continuous wave solid-state laser source (TruDisk 4001, Germany), a coaxial powder feeding system (RC-PGF-D, China), an ABB robot (IRB4600-60, Sweden). The wavelength and spot diameter of the laser beam are 1,030 nm and 2 mm, respectively. The defocus distance is set to 10 mm. The process parameters used in the experiments are listed in Table 1. The fabricated single tracks are shown in Fig. 1(c), from which it can be seen that all the single tracks are free of macroscopic metallurgical defects. Fig. 1(d) shows the typical cross-sectional morphology of single track, which is composed of molten pool, heat affected zone, and substrate (unlabeled in this figure).

In the present work, a laser energy density (LED, J/mm^2) was introduced to characterize the effects of the laser power and laser scanning speed on the microstructures and mechanical properties of LDED-fabricated single tracks of the CoCrNi MEA, which is expressed as follows:

$$LED = \frac{P}{d \times v} \tag{1}$$

where P is the laser power, d is the diameter of the laser spot, and v is the laser scanning speed.

2.2. Microstructural characterization and hardness tests

Based on the above LDED process parameters, six single tracks with a length of about 40 mm were obtained. To clarify the microstructural evolution of the single tracks, all single tracks were cut perpendicularly to the laser moving direction to prepare metallographic samples. Then the samples were carefully polished and chemically etched with a metallographic etching solution of 3 ml HCl + 1 ml HNO_3 + 4 ml deionized water. The microstructure and elemental distribution of samples were characterized by a scanning electron microscope (SEM, Zeiss Supra55) equipped with an electron backscattered diffraction (EBSD) detector. The average size of cells was determined with the Heyn linear intercept method [23]. Transmission electron microscope (TEM, FEI Talos F200x) was conducted to reveal the dislocation density of the as-fabricated samples. Finally, the hardness measurements were performed, using a Vickers hardness tester (HuaYin, HVS-1000B), with a load of 300 g and a dwell time of 15 s.

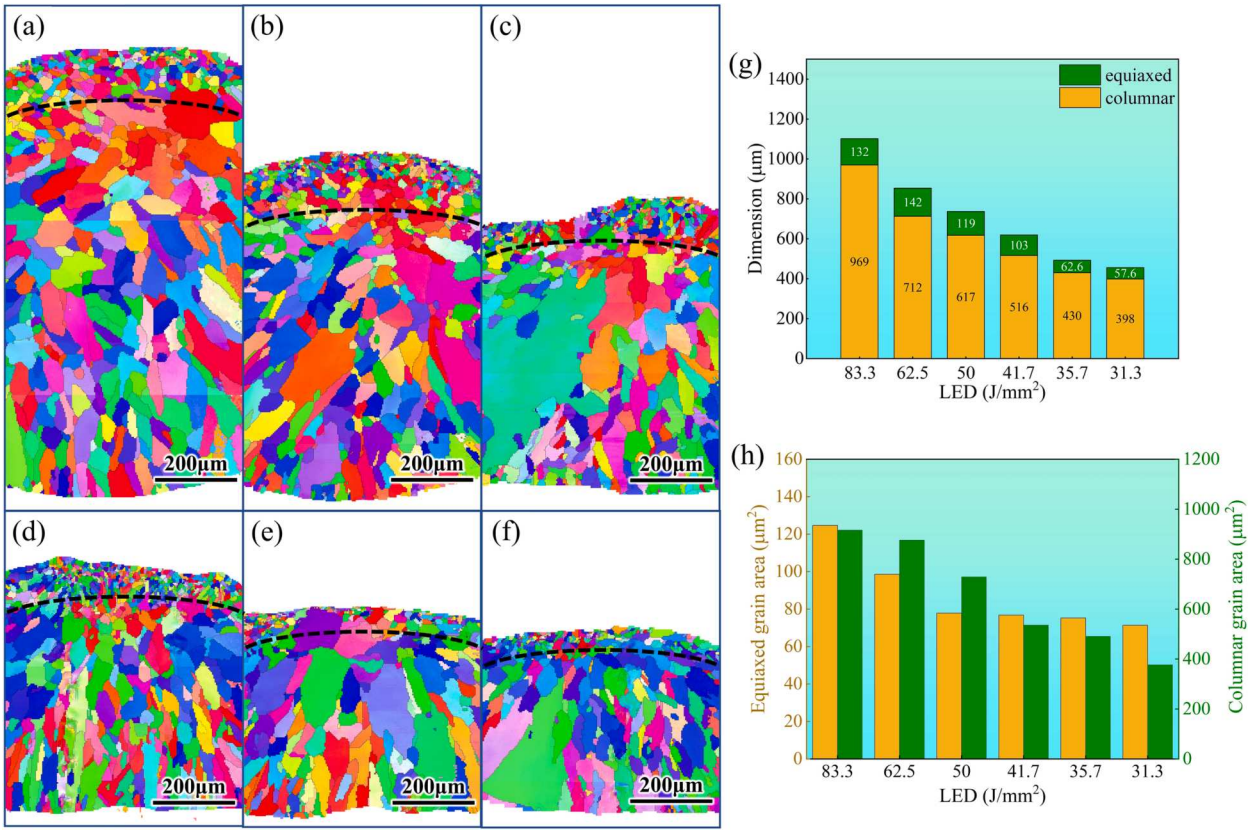

Fig. 2. EBSD images of the single tracks of the CoCrNi MEA fabricated by different LED: (a) 83.3 J/mm^2, (b) 62.5 J/mm^2, (c) 50 J/mm^2, (d) 41.7 J/mm^2, (e) 35.7 J/mm^2, and (f) 31.3 J/mm^2. The black dotted line is the boundary between the equiaxed grain layer and the columnar grain layer. (g) The measured thickness of the equiaxed grain layer and columnar grain layer. (h) The average grain area of equiaxed grains and columnar grains.

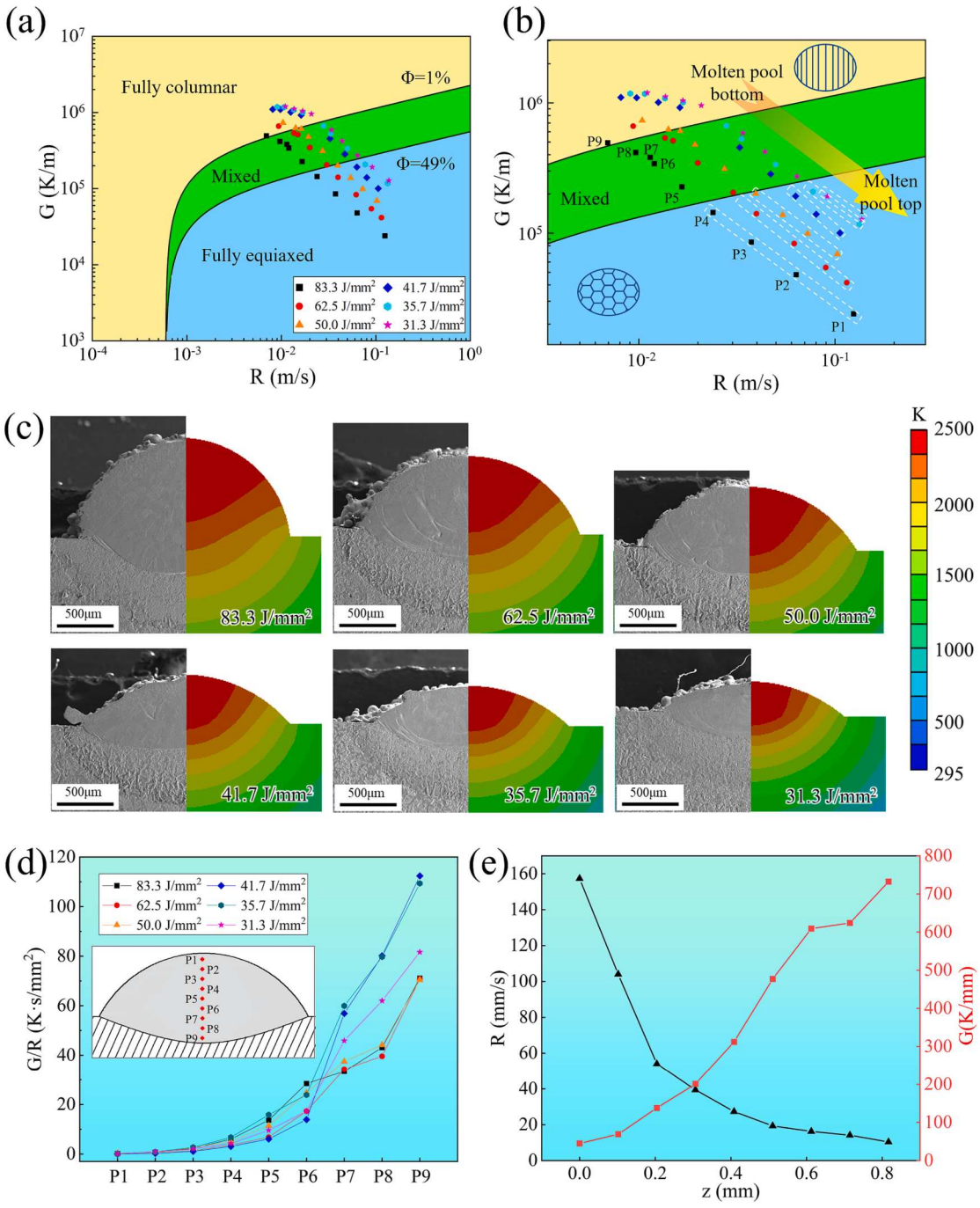

Fig. 3. (a) CET map for LDED-fabricated CoCrNi MEA and (b) enlarged image. (c) The simulated temperature field corresponds to the experimental molten pool at the cross-section of single tracks fabricated by different LED. (d) The evolution of G/R from P1 to P9. (e) Evolution of G and R as the depth z ($z = 0$ corresponding to the surface) of the single track formed by a LED of 50 J/mm^2. The white rectangles in (b) show the shifted monitoring points. The inserted image in (d) shows the distribution of test points for monitoring solidification conditions (G and R) in the molten pool.

2.3. Mathematical model

To study the effect of LED on the microstructures and mechanical properties of LDED-fabricated single tracks of the CoCrNi MEA, a transient heat transfer model based on the finite element (FE) theory was used to study the temperature evolution of single tracks during the LDED process.

For this simulation, the following assumptions were adopted to simplify the calculation: (i) the materials were assumed to be isotropic and homogeneous; (ii) the flow of the liquid phase in the molten pool was ignored; and (iii) the thermal properties used for the calculation were considered to be temperature dependent.

The parameters used for the FE calculations were listed in Table 2. The materials properties of the substrate (45# steel) and CoCrNi MEA were presented in Table 3. The three-dimensional models used for FE calculations were established by comparing the dimension of the single tracks.

The laser energy was employed by a moving heat flux with a Gaussian distribution, and can be defined as follows:

$$Q = \frac{2\alpha P}{\pi r_0^2} exp\left(-\frac{2r^2}{r_0^2}\right) \tag{2}$$

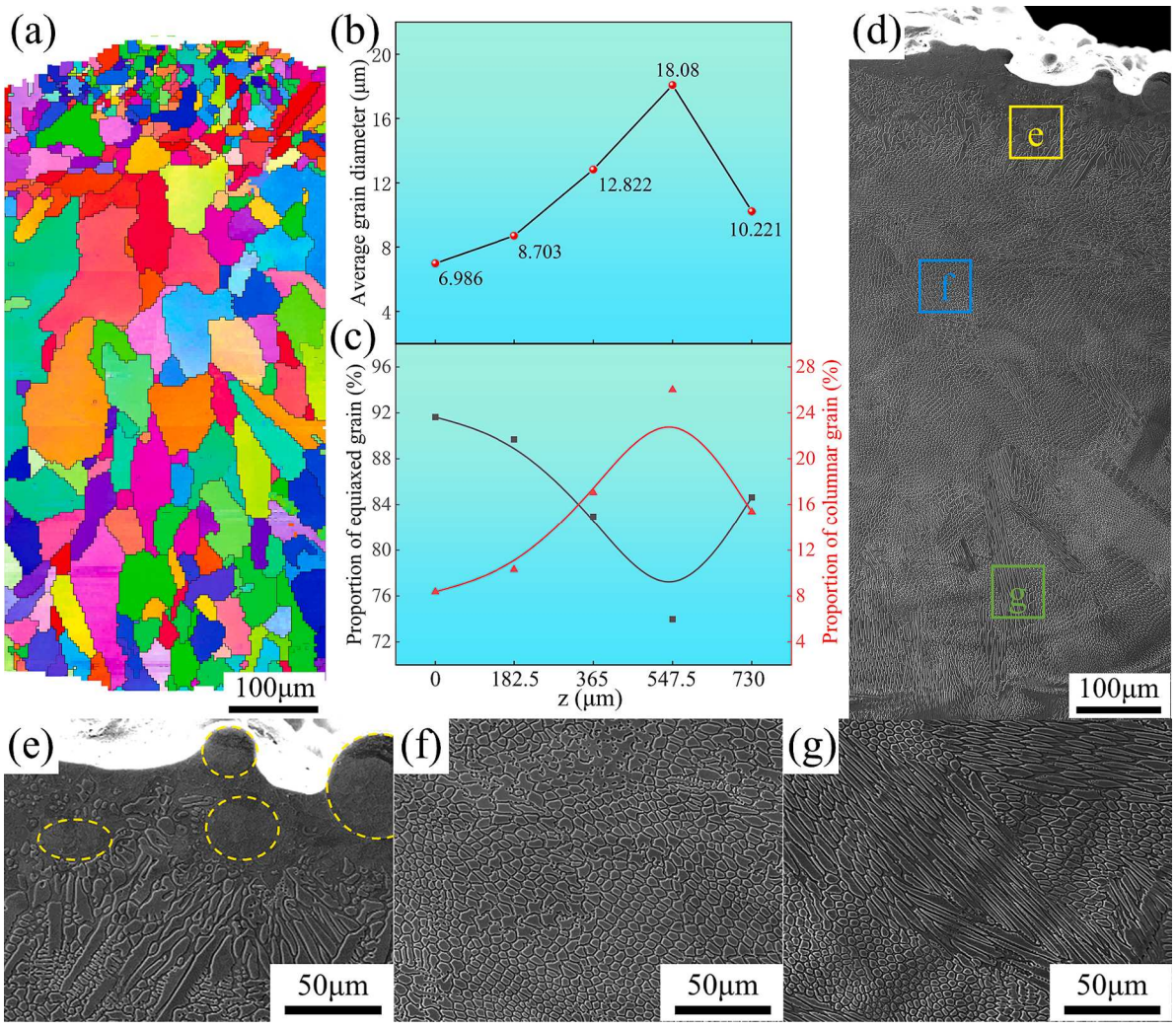

Fig. 4. The cross-sectional microstructure of the single track of the CoCrNi MEA fabricated by a LED of 50 J/mm^2. (a) is the EBSD image along the deposition height. (b) and (c) are the average grain diameter, and proportion of equiaxed and columnar grain at different deposition height ($z = 0$ corresponding to the surface), respectively. (d) is the SEM image along the deposition height. (e-g) are the enlarged SEM images of the corresponding regions marked in (d), respectively.

where α is the laser absorption coefficient, P is the laser power, r_0 is the radius of the laser beam, and r is the distance from the radiant point to the center of the laser beam.

The spatial and temporal distributions of the transient temperature field were obtained by solving the transient nonlinear heat-transfer equation, which is described as follows [24]:

$$\rho c\left(\frac{\partial T}{\partial t}\right)=\frac{\partial}{\partial x}\left(k\frac{\partial T}{\partial x}\right)+\frac{\partial}{\partial y}\left(k\frac{\partial T}{\partial y}\right)+\frac{\partial}{\partial z}\left(k\frac{\partial T}{\partial z}\right)+Q \tag{3}$$

where ρ is the density, c is the specific heat, k is the thermal conductivity, Q is the input heat, T is the node temperature, and t is the time.

In general, the heat exchange between the materials and the environment during the LDED process can be divided into the heat conduction (q_{cond}), heat convection (q_{conv}), and heat radiation (q_r). Accordingly, the boundary condition for the FE calculation can be expressed as follows [25]:

$$q_{cond}=k(T_{mol}-T_0) \tag{4}$$

$$q_{conv}=h(T_{mol}-T_0) \tag{5}$$

$$q_r=\sigma\varepsilon\left(T_{mol}^4-T_0^4\right) \tag{6}$$

where h is the convection heat-transfer coefficient, σ is the Stefan-Boltzmann constant, ε is the surface emissivity, Q is the input heat, T_{mol} is the temperature of the molten pool, and T_0 is the environmental temperature.

3. Results and discussion

3.1. Effect of LED on the evolution of CET

The EBSD was used to characterize the grain distribution of single tracks formed by different LED, and the corresponding images are shown in Fig. 2(a-f). It can be clearly seen that all the as-built single tracks exhibit the CET behavior. According to Hunt criterion [22], the grains with an aspect ratio between 0 and 2 are classified as equiaxed grains, and those larger than 2 are columnar grains. Based on this, the area where the proportion of equiaxed grains is greater than 90 % is considered as equiaxed grain layer and the rest is columnar grain layer. The boundary is shown as the black dotted line in Fig. 2(a-f). As the LED decreases from 83.3 J/mm^2 to 31.3 J/mm^2, the thickness of the equiaxed grain layer gradually decreases from ~ 132 μm to ~ 57.6 μm (Fig. 2g). The average grain area of the equiaxed grain and columnar grain also decreases with decreasing LED (Fig. 2h).

To clarify the effect of LED on the variation of the CET, a solidification model established by Gäumann was employed to depict the CET map of the LDED-fabricated CoCrNi MEA, which can be expressed as

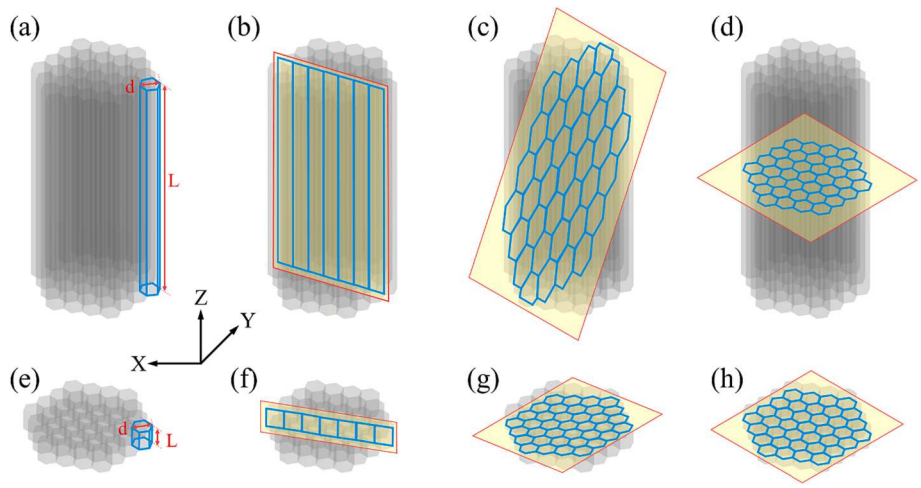

Fig. 5. Schematic diagrams of different views of columnar cells. (a) and (e) are the cluster of parallel columnar cells with different cell length *L*. (b) and (f) are section along the XZ plane. (c) and (g) are the section along the longest diagonal of cluster. (d) and (h) are section along the XY plane.

follows [27]:

$$G = \frac{1}{n+1}\sqrt[3]{\frac{-4\pi}{3ln(1-\varphi)}}N_0^{\frac{1}{3}}\left(1-\frac{\Delta T_n^{n+1}}{(aR)^{\frac{n+1}{n}}}\right)(aR)^{\frac{1}{n}} \tag{7}$$

where G is the temperature gradient, φ is the volume fraction of equiaxed grains, N_0 is the nucleation density, ΔT_n is the nucleation undercooling, R is the solidification rate, a and n are the material-dependent constants. In the case of the high G induced by the LDED process, the nucleation undercooling ΔT_n can be neglected in this calculation. Thereby, the CET model can be simplified as follows:

$$\frac{G^n}{R} = a\left[\sqrt{3}\frac{-4\pi N_0}{3ln(1-\varphi)}\frac{1}{1+n}\right]^n \tag{8}$$

The values of a and n can be calculated, using Lin's model developed by extending Gäumann's model [28]. Here, a was defined as 1.25×10^6 $K^m{\cdot}s{\cdot}m^{-1}$, and n was defined as 3.4. According to the work by Greer et al. [29], the nucleation density N_0 can be estimated by:

$$N_0 = \frac{0.5}{\omega^{-3}} \tag{9}$$

where ω represents the average grain size and can be obtained from the EBSD data. Hunt et al. [22] proposed that the formation of fully equiaxed grains occurs if the volume fraction of equiaxed grains $\varphi > 0.49$, whereas the solidification microstructure is assumed to be fully columnar grains if $\varphi < 0.01$. Thus, the critical φ values for the LDED-fabricated CoCrNi MEA are defined as 49 % and 1 %, respectively. Combining Eq. (7), (8), and (9), the CET map of the CoCrNi MEA was calculated as presented in Fig. 3(a) and 3(b), separated into three regions corresponding to different grain morphologies: a fully columnar region, fully equiaxed region, and mixed columnar-equiaxed region. Fig. 3(c) shows the simulated temperature field corresponding to the experimental molten pool at the cross-section of single tracks fabricated by different LED. Additionally, the G and R of the monitoring points shown in inserted image in Fig. 3(d) were extracted from a simulated temperature field and marked in the CET maps. As illustrated in Fig. 3 (a), the solidification conditions of the equiaxed grain region are with low G ($\sim 10^4$ K/m) and high R ($\sim$0.1 m/s) whereas the solidification conditions of the columnar grain region are high G ($\sim 10^6$ K/m) and low R ($\sim$0.01 m/s). It was well known that the morphology of the solidified grains is determined by the ratio of G/R and the high G/R is beneficial to form columnar grains whereas the equiaxed grains usually generated at low G/R. As seen in Fig. 3 (d), for every single track, the ratio of G/R continues to increase with the monitoring points shifts from P1 to P9, suggesting the equiaxed grains tend to generate at the top of the molten whereas the columnar grains tend to form at the bottom of the molten pool. This simulated result well explains the reasons for the distribution of different morphological grains and simultaneously confirm the CET occurring along the deposition direction was driven by the changes in temperature conditions. Furthermore, as shown in Fig. 3(b), the decreasing LED shifts the position of P1 to P9 from the equiaxed grain region towards the mixed/columnar grain region, causing a thin equiaxed grain layer. This phenomenon agrees well with the experimental results shown in Fig. 2, confirming the validity of FE simulation results and the CET map proposed for the LDED-fabricated CoCrNi MEA. Here, single tracks fabricated by 50 J/mm^2 was chosen to show the evolution of G and R as the deposition height z ($z = 0$ corresponding to the surface). As shown in Fig. 3(e), with increasing z, G gradually increases whereas R gradually decreases.

3.2. Microstructure characteristics of single track

Fig. 4 shows the cross-sectional microstructures of the single track formed by a LED of 50 J/mm^2. As shown in Fig. 4(a), the size and morphology of grains inside the molten pool is closely related to the deposition height. In order to accurately analyze the distribution of grains, the detailed data was abstracted from EBSD results. As shown in Fig. 4(b) and (c), finer equiaxed grains form at the top of the molten pool whereas the columnar grains with a larger size form at the middle and bottom of the molten pool, suggesting that the CET occurs along the deposition height.

Fig. 4(d) shows the etched microstructure of the molten pool. It can be seen that the etched microstructure is also correlated with the deposition height. Fig. 4(e-g) show the enlarged SEM images at the top, middle, and bottom of Fig. 4(d), respectively. At the surface of the molten pool, some incompletely melted powders are visible (Fig. 4e), which can be attributed to the insufficient laser energy or excess powder feed rate [30]. When it comes to stable solidification region, the solidification structure with equiaxed cells can be observed in the top and middle of the molten pool (Fig. 4f) whereas equiaxed, elongated, and columnar cells present at the bottom of the molten pool (Fig. 4g), which has been widely reported in many studies of additive manufacturing [31,32].

Comparing the EBSD image (Fig. 4a) and SEM image (Fig. 4d), it can be found that the structural coherence of cells within each grain in EBSD image, which indicates that the cells observed in SEM are not independently grains with different orientation but rather substructures with same orientation. This result is consistent with the work proposed by

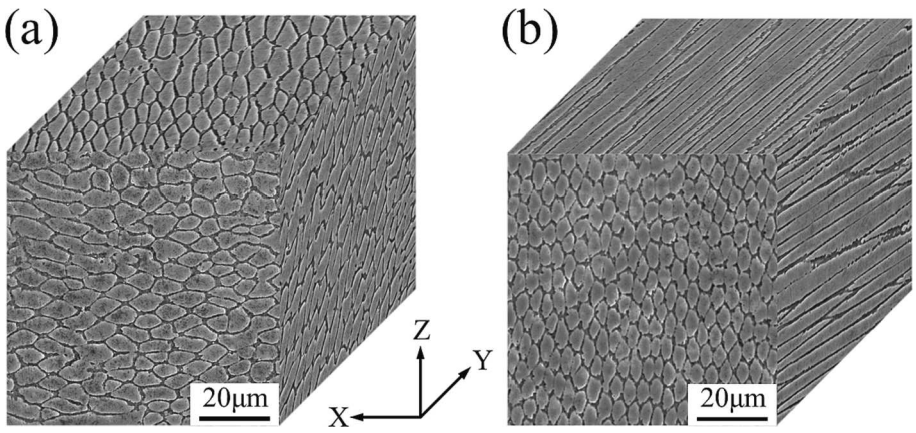

Fig. 6. Three-dimensional solidification structures of region f and region g marked in Fig. 4(d). (a) Region f. (b) Region g. X is the transverse direction, Y is the scanning direction, and Z is the deposition height.

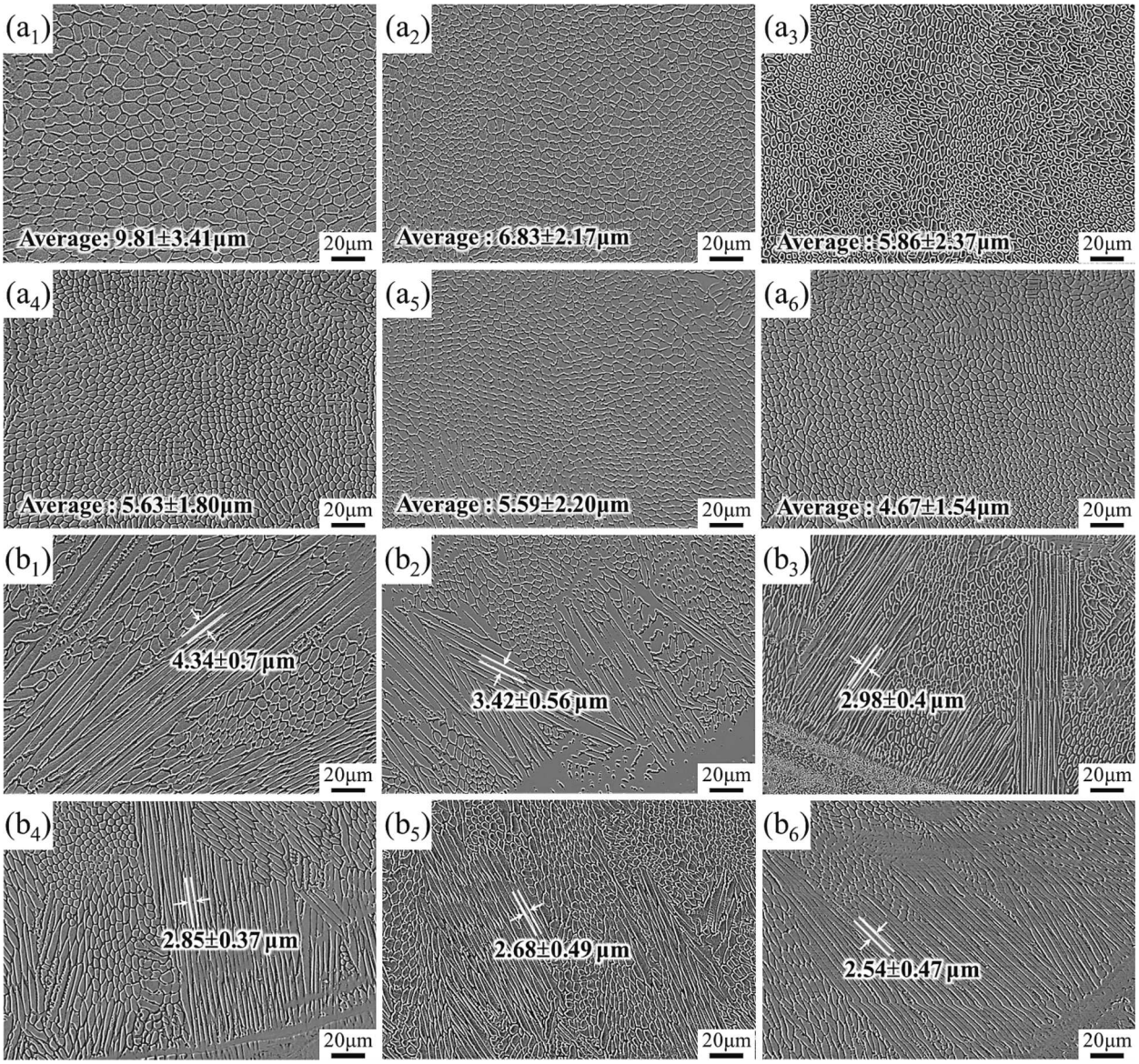

Fig. 7. The cross-sectional substructure of (a) equiaxed cells and (b) columnar cells formed by different LED: (a_1, b_1) 83.3 J/mm^2, (a_2, b_2) 62.5 J/mm^2, (a_3, b_3) 50 J/mm^2, (a_4, b_4) 41.7 J/mm^2, (a_5, b_5) 35.7 J/mm^2, and (a_6, b_6) 31.3 J/mm^2. The average size of equiaxed cells and the average width of columnar cells are marked in black font.

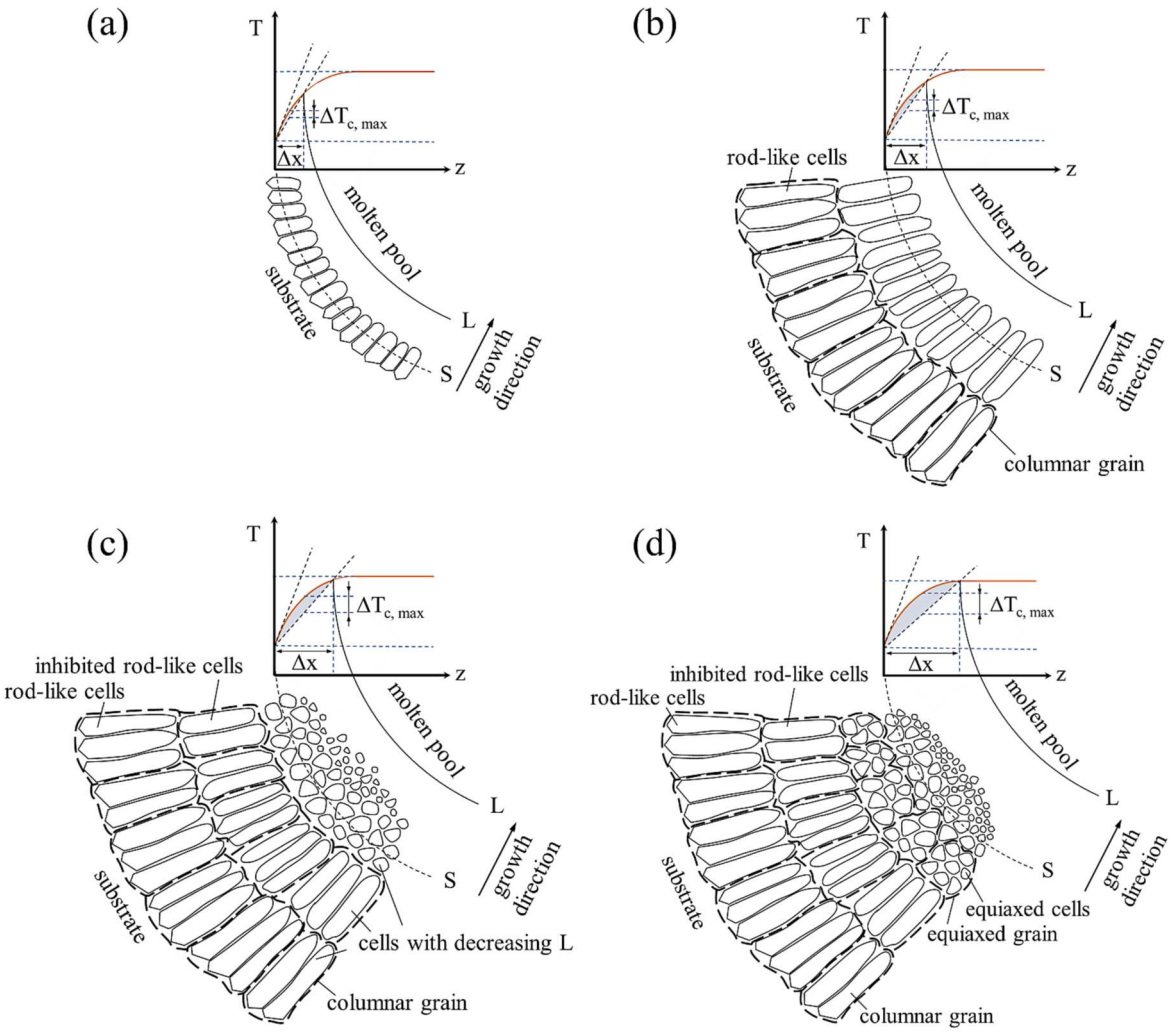

Fig. 8. The schematic illustration of the morphological transformation of cells observed in the LDED-fabricated single tracks of CoCrNi MEA: (a) Stage I: the formation of primary cells. (b) Stage II: the formation of rod-like cells with high *L*. (c) Stage III: the formation of inhibited rod-like cells and the nucleation of cells with decreasing *L*. (d) Stage IV: the formation of fine cells with equiaxed.

Wei et al. [33]. As for different substructure morphologies shown in Fig. 4(f) and (g), Pham et al. [31] suggested that it is related to the view direction of the columnar cells, like the schematics shown in Fig. 5. As shown in Fig. 5(a) and (e), the grain in EBSD image was assumed to be a cluster with some directionally arranged rod-like cells. The cross-sectional diameter of single cell is *d*, and the length of cell is *L*. For the cells with high aspect ratio ($L/d > 2$) as shown in Fig. 5(a), the cross-sectional morphologies exhibit as directional arranged columnar cells (Fig. 5b), elongated cells (Fig. 5c) and equiaxed cells (Fig. 5d) in different direction, which are consistent of the solidification structures shown in Fig. 4(g) and indicate that the rod-like cells at the bottom of the molten pool are randomly arranged in space. Conversely, when the aspect ratio of cells is less than 2, such as equal to 1, the cross-sectional morphologies exhibit as equiaxed cells in all directions as shown in Fig. 5(f-h). Based on the above analysis and combined with the EBSD and SEM images in Fig. 4, it is presumed that the equiaxed grains in the molten pool consist of low aspect ratio cells ($L/d < 2$) whereas the columnar grains consist of high aspect ratio cells ($L/d > 2$). To verify this conjecture, three-dimensional structures of cells in the middle and bottom of the molten pool were performed, as shown in Fig. 6. The exhibited structures of cells agree well with the schematics shown in Fig. 5(a) and (e), which proves that the above conjecture is accurate. Therefore, it can be concluded that the observed CET along the deposition height is occurred as a result of the variation in the aspect ratio of rod-like cells.

Relying on the above conclusions, the connection between cells and the CET can be established. As shown in Fig. 5, the aspect ratio of single grain (R_{as}), which determines the morphology of the grain, can be expressed as follows:

$$R_{as} = \frac{L}{\tau \times d} \tag{10}$$

where τ is number of cells. According to Eq. (10), for a fixed τ, the aspect ratio of grain is proportional to the L/d. Meanwhile, the grain volume (V_{gr}) is also determined by the *d* and *L* of the cells, and can be calculated by the follows:

$$V_{gr} = \tau \times d \times L \tag{11}$$

According to Eq. (10) and (11), the *d* and *L* of cells play an important role in the CET and grain size. In order to achieve a tunable CET, it is meaningful to investigate the growth condition of *d* and *L*. During the LDED process, the *L* of cell is parallel to the epitaxial growth direction and can continuously grow along the direction perpendicular to the solid–liquid interface [34]. However, *d* of cell is limited by the cell spacing and cannot grow continuously. Consequently, *L* plays a more important role than *d* in controlling the CET and grain size. In the subsequent analysis, the attention will be focused on the growth condition of *L* and morphological transformation of cells.

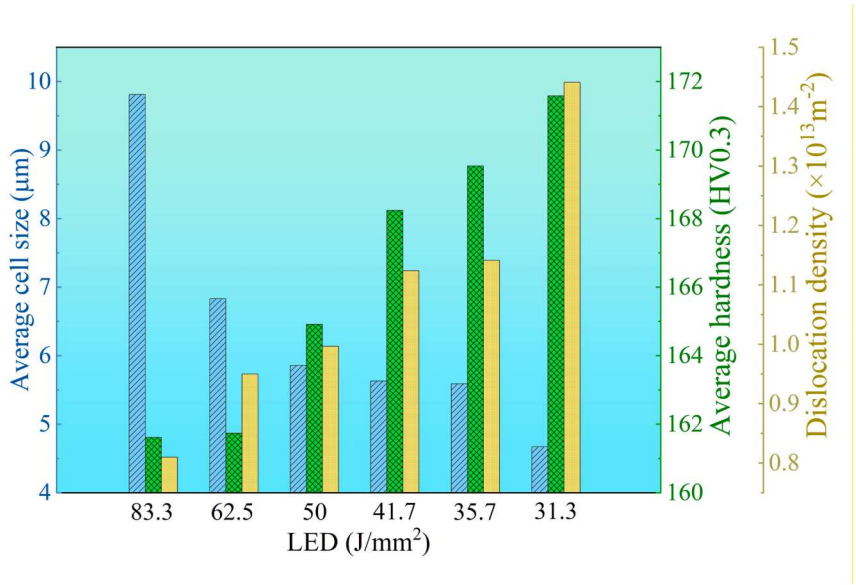

Fig. 9. The variation of the average cell size, dislocation density, and average hardness of single tracks as a function of LED.

3.3. Morphological transformation mechanism of the substructure

The cross-sectional substructure of single tracks formed by different LED is shown in Fig. 7. As seen, the morphological transformation of cells from an equiaxed to elongated shape can be observed in every single track. Relevant studies have proved that the morphological transformation of the solidification substructure is closely related to the constitutional undercooling ahead of the solid–liquid interface [35–37]. Combining FE simulations, experimental characterizations, and compositional undercooling theory, as shown in Fig. 8, a schematic illustration was depicted to clarify the mechanism of morphological transformation of cells which is responsible for the CET observed in the LDED-fabricated CoCrNi MEA.

During the LDED process, the initial solidification starts at the bottom of the molten pool. Since the bottom of the molten pool is welded to the cooling substrate, the heat dissipates downwards through the substrate, resulting in a high G. Due to the high G, the region of constitutional undercooling (Δx) generated ahead of the solid–liquid interface is narrow and the maximum value of constitutional undercooling ($\Delta T_{c,max}$) is low. In this case, the newly formed substructures at the bottom of the molten pool grow in a cellular morphology as shown in Fig. 8(a). With the help of directional heat dissipation existed in the molten pool boundary, these newly formed cells will epitaxially grow in the direction perpendicular to the molten pool boundary, consequently forming rod-like cells with high aspect ratio (Fig. 8b).

When the solidification progresses to the center of the molten pool,

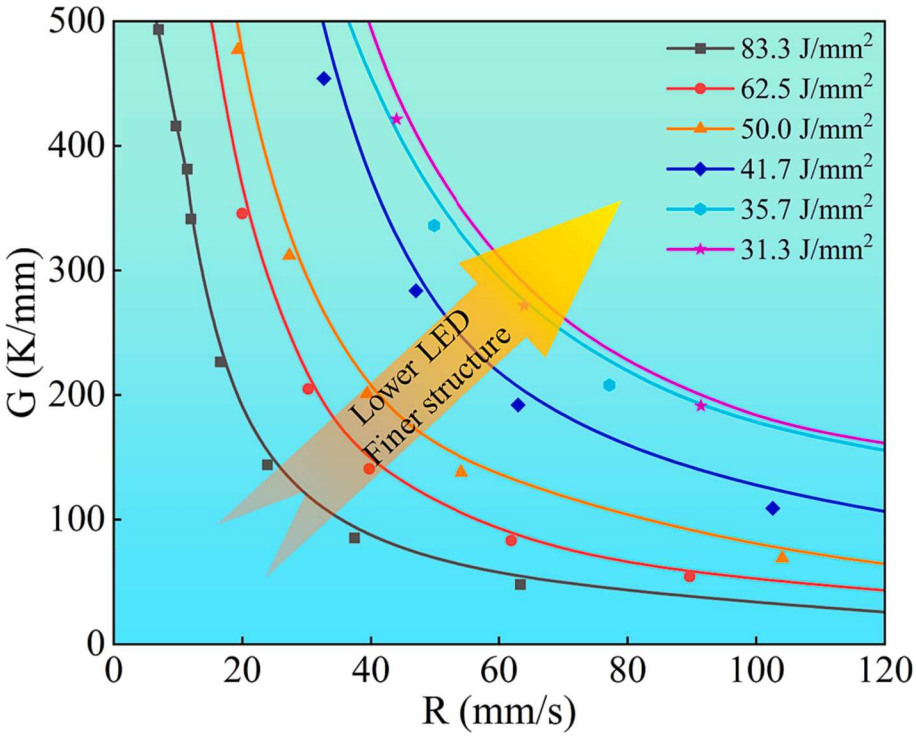

Fig. 10. The *G-R* map of LDED-fabricated single tracks formed by different LED.

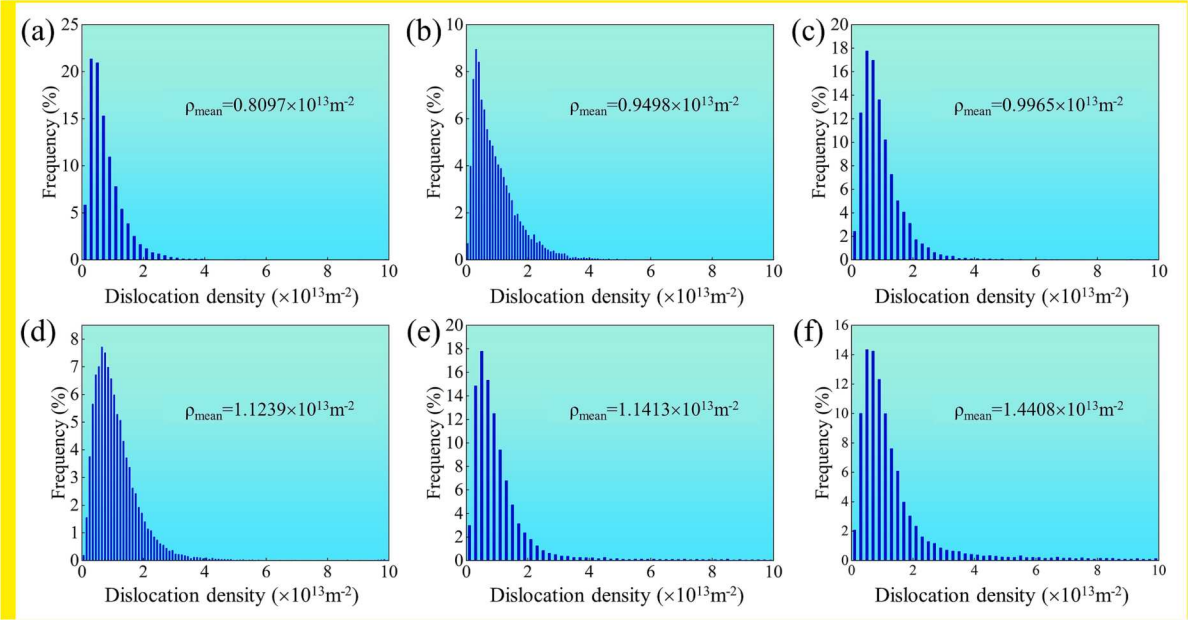

Fig. 11. The calculated dislocation density distribution of the single tracks of the CoCrNi MEA formed by different LED: (a) 83.3 J/mm^2, (b) 62.5 J/mm^2, (c) 50 J/mm^2, (d) 41.7 J/mm^2, (e) 35.7 J/mm^2, and (f) 31.3 J/mm^2.

the G ahead of the solid–liquid interface further decreases (Fig. 3e), generating a wider Δx and a larger $\Delta T_{c,\,max}$. In this case, larger $\Delta T_{c,\,max}$ will surpass the critical undercooling (ΔT_{cn}) required for heterogeneous nucleation, resulting in a great increase in the number of nuclei sites [38–40]. Plenty of newly formed cells become competitive than former cells and block the epitaxial growth of the rod-like cells (Fig. 8c). With decreasing G and increasing nuclei sites, the L of cells gradually decrease, and the cells with low aspect ratio formed, resulting in the morphological transformation of cells. Meanwhile, the newly formed cells were gradually finer due to the increasing R and nuclei sites. As the solidification proceeds further towards the surface of the molten pool, the R reaches the maximum and the G reaches the minimum. The explosive nucleation occurs within the molten pool, and the fine equiaxed cells formed as shown in Fig. 9(d).

For different single tracks, the variation of G and R is mainly determined by the LED used for LDED process. As shown in Fig. 3(b), the G in the single track formed by a LED of 83.3 J/mm^2 is lower at every monitoring point than the others. In this case, the maximum value of undercooling ahead of the solid–liquid interface will easily exceed the critical nucleation undercooling earlier due to the lower G at P9 corresponding to the bottom of the molten pool, which means the epitaxial growth of the rod-like cells will be blocked by the newly formed cells. When the LED is reduced, the G at P9 of the molten pool gradually increases. Due to this variation, the resistance to epitaxial growth of the cells gradually decreases. As a consequence, the proportion of cells with high aspect ratio in the molten pool will gradually increase whereas the proportion of cells with low aspect ratio will gradually decrease. That is, as the LED decreases, CET becomes difficult to occur.

3.4. Relationship between microstructure features and hardness

After the microstructure analysis, the relationship between microstructure and hardness was discussed in this section. Fig. 9 shows the average size of equiaxed cells, dislocation density, and average hardness of different single tracks. With the decrease of LED, the average hardness obtained from the cross-section of the single tracks gradually increases, which are 161.1 $HV_{0.3}$, 161.7 $HV_{0.3}$, 164.9 $HV_{0.3}$, 168.2 $HV_{0.3}$, 169.5 $HV_{0.3}$, and 171.6 $HV_{0.3}$, for 83.3 J/mm^2, 62.5 J/mm^2, 50 J/mm^2, 41.7 J/mm^2, 35.7 J/mm^2 and 31.3 J/mm^2, respectively. Generally, the hardness of metallic alloys is mainly determined by the microstructure features [41–43]. In the current work, the higher hardness of LDED-fabricated single tracks at a lower LED can be attributed to the fine cells and high dislocation densities.

Compared to the G-R map developed by Kou et al. [44], the G-R map for the LDED-fabricated CoCrNi MEA was depicted in Fig. 10. It can be found that the $G \times R$ which means that the cooling rate increases with decreasing LED, which favors the formation of the fine cells. As shown in Fig. 7, the average size of equiaxed cells gradually decreases from 9.81 ± 3.41 μm to 4.67 ± 1.54 μm and the average width of columnar cells decreases from 4.34 ± 0.7 μm to 2.54 ± 0.47 μm with the decrease of LED from 83.3 J/mm^2 to 31.3 J/mm^2. The relationship between the hardness and the average cell size can be described using the normal Hall-Petch relationship theory [45]:

$$H = H_0 + \frac{K_y}{\sqrt{\omega}} \tag{12}$$

where H is the hardness, ω is the average cell size, H_0 represents the value of friction hardness and is a constant independent of grain size, and K_y is the slope of Hall-Petch relations. According to Eq. (12), the hardness values are inversely proportional to the average cell size. Thus, a decrease in the LED causes a higher hardness for the single tracks of the CoCrNi MEA via finer cells.

The role of dislocations is achieved by increasing the deformation resistance of the metallic alloys to inhibit the moving indenter, leading to increased hardness. Many literatures have revealed that the dislocation density in LDED-fabricated parts is determined by the cooling rate [46,47]. Due to the high cooling rate, the thermal expansion and shrinkage of the material have not enough time to come to an equilibrium state, which results in a considerable localized strain. To accommodate the local strain, micro deformation will operate by dislocation motion and cause a high dislocation density in the fabricated parts. Here, the dislocation density of single tracks was calculated based on the strain gradient theory, which is expressed as follows [48,49]:

$$\rho = \frac{2\theta}{\mu b} \tag{13}$$

where ρ is the dislocation density at the point of interest, θ represents the

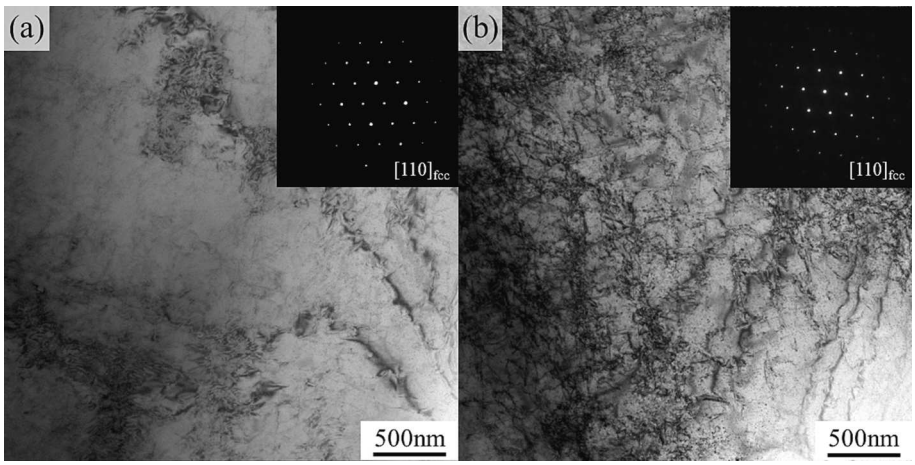

Fig. 12. Bright-field TEM images of the single tracks of the CoCrNi MEA formed by different LED: (a) 83.3 J/mm^2, (b) 31.3 J/mm^2. The inset shows the corresponding SAED pattern.

local misorientation angle, μ is the unit length (3.2 μm) of the point, and b is the Burger's vector (0.253 nm for CoCrNi MEA [50]). As shown in Fig. 11, the calculated dislocation density of single tracks increases with decreasing LED, increasing from 0.8097 × 10^{13} m^{-2} at 83.3 J/mm^2 to 1.4408 × 10^{13} m^{-2} at 31.3 J/mm^2. To further confirm the relationship between the dislocation density of single tracks and LED, the bright-field (BF) TEM images corresponding to the single tracks formed by 83.3 J/mm^2 and 31.3 J/mm^2 were taken along the [1 1 0] zone axis. As shown in Fig. 12, the single track formed by 31.3 J/mm^2 has a higher dislocation density than the single track formed by 83.3 J/mm^2, and dislocation pile-ups can be seen in the Fig. 12(b) which causes a high hardness via the dislocation strengthening effect.

4. Conclusions

In the present work, the LDED technique was conducted to fabricate single tracks of a CoCrNi MEA by different LED. Combining finite element simulations and experimental characterizations, the effect of LED on the CET and morphological transformation of substructure occurred in the as-built CoCrNi MEA were studied, providing necessary theoretical guidance for fabricating MEAs. The main conclusions are described as follows:

(1) All the as-built single tracks present the CET along the deposition height. The CET map established for the as-built CoCrNi MEA shows that the evolution of the CET can be attributed to the variation of G and R within the molten pool. The decreased LED can inhibit the CET and cause the thickness of an equiaxed grain layer gradually to decrease from ~ 132 μm at 83.3 J/mm^2 to ~ 57.6 μm at 31.3 J/mm^2.
(2) The grains in molten pool were composed of some directionally arranged rod-like cells. The equiaxed grains in the molten pool consist of low aspect ratio cells ($L/d < 2$) whereas the columnar grains consist of high aspect ratio cells ($L/d > 2$). As a result of the morphological transformation of cells, the CET occurs with the increase of deposition height.
(3) The epitaxial growth plays an important role in controlling the aspect ratio of cells, which is critically controlled by the constitutional undercooling in the molten pool. Increasing LED can lead to a large undercooling degree and a wide undercooling zone with a promoted heterogeneous nucleation that inhibits the epitaxial growth of cells by competitive growth between former cells and newly formed cells.
(4) The fine cells and high dislocation density caused by the high cooling rate during LDED process were responsible for the increased hardness of single tracks. By substructure refinement and dislocation strengthening, the average hardness of the single tracks increases from 161.1 $HV_{0.3}$ at 83.3 J/mm^2 to 171.6 $HV_{0.3}$ at 31.3 J/mm^2.

Furthermore, this work still has limitations. The laser power and scanning speed are two main effect factors for LED. The experimental design of this work only changes the scanning speed and the laser power is constant, which does not fully reflect the effect of LED on the CET. To further refine this work, we will change the laser power for forming single tracks and explores the corresponding CET behavior in the next work. Besides, as reported by many works, secondary phases also have an influence on the CET behavior. Thus, in the future, we will also discuss this influence.

Declaration of competing interest

The authors declare that they have no known competing financial interests or personal relationships that could have appeared to influence the work reported in this paper.

Data availability

Data will be made available on request.

Acknowledgements

The authors would like to acknowledge the financial support from Guangdong Major Project of Basic and Applied Basic Research (2020B0301030001), Shenzhen Fund 2021 Basic Research General Programme (project code: JCYJ20210324115400002)], National Key R&D Programme, Ministry of Science and Technology of China under grant No. 2019YFA0209904, CGN-HIT Advanced Nuclear and New Energy Research Institute (Grant No. CGN-HIT202209), and the National Natural Science Foundation of China under Grant Nos. 52371106, and 52371025. PKL very much appreciates the support from (1) the National Science Foundation (DMR-1611180, 1809640, and 2226508) and (2) the US Army Research Office (W911NF-13-1-0438 and W911NF-19-2-0049).

References

[1] Y. Zhang, T.T. Zuo, Z. Tang, M.C. Gao, K.A. Dahmen, P.K. Liaw, Z.P. Lu, Microstructures and properties of high-entropy alloys, Prog. Mater. Sci. 61 (2014) 1–93.

[2] Y. Tang, R.X. Wang, B. Xiao, Z.R. Zhang, S. Li, J.W. Qiao, S.X. Bai, Y. Zhang, P. K. Liaw, A review on the dynamic-mechanical behaviors of high-entropy alloys, Prog. Mater. Sci. 135 (2023), 101090.
[3] W.D. Li, D. Xie, D.Y. Li, Y. Zhang, Y.F. Gao, P.K. Liaw, Mechanical behavior of high-entropy alloys, Prog. Mater. Sci. 118 (2021), 100777.
[4] B. Gludovatz, A. Hohenwarter, K.V. Thurston, H. Bei, Z. Wu, E.P. George, R. O. Ritchie, Exceptional damage-tolerance of a medium-entropy alloy CrCoNi at cryogenic temperatures, Nat. Commun. 7 (2016) 10602.
[5] G. Laplanche, A. Kostka, C. Reinhart, J. Hunfeld, G. Eggeler, E.P. George, Reasons for the superior mechanical properties of medium-entropy CrCoNi compared to high-entropy CrMnFeCoNi, Acta Mater. 128 (2017) 292–303.
[6] S.H. Yoshida, T. Bhattacharjee, Y. Bai, N. Tsuji, Friction stress and Hall-Petch relationship in CoCrNi equi-atomic medium entropy alloy processed by severe plastic deformation and subsequent annealing, Scr. Mater. 134 (2017) 33–36.
[7] B. Gan, J.M. Wheeler, Z.N. Bi, L.J. Liu, J. Zhang, H.Z. Fu, Superb cryogenic strength of equiatomic CrCoNi derived from gradient hierarchical microstructure, J. Mater. Sci. Technol. 35 (6) (2019) 957–961.
[8] C.E. Slone, S. Chakraborty, J. Miao, E.P. George, M.J. Mills, S.R. Niezgoda, Influence of deformation induced nanoscale twinning and FCC-HCP transformation on hardening and texture development in medium-entropy CrCoNi alloy, Acta Mater. 158 (2018) 38–52.
[9] Z.Y. Liu, X.Y. Zhao, Y.W. Wu, Q. Chen, B.H. Yang, P. Wang, Z.W. Chen, C. Yang, Homogenization heat treatment for an additively manufactured precipitation-hardening high-entropy alloy, Rare Met. 41 (2022) 2853–2863.
[10] A.N. Alagha, S. Hussain, W. Zaki, Additive manufacturing of shape memory alloys: A review with emphasis on powder bed systems, Mater. Design 204 (2021), 109654.
[11] S.E. Alkhatib, T.B. Sercombe, High strain-rate response of additively manufactured light metal alloys, Mater. Des. 217 (2022), 110664.
[12] W. Zhang, A. Chabok, B.J. Kooi, Y.T. Pei, Additive manufactured high entropy alloys: A review of the microstructure and properties, Mater. Des. 220 (2022), 110875.
[13] B.S. Guan, M.G. Xu, X.S. Yang, Y.Z. Zhou, C. Li, Y.Q. Ji, X.J. Liu, J.F. Li, D. Wang, J. G. Tang, G.M. Le, Microstructure and strengthening mechanisms of tantalum prepared using laser melting deposition, Int. J. Refract. Met. Hard Mater. 103 (2022), 105773.
[14] Y.T. Su, Y.C. Wang, J. Shi, Microstructure and mechanical properties of laser DED produced crack-free Al 7075 alloy: Effect of process parameters and heat treatment, Mater. Sci. Eng. A 857 (2022), 144075.
[15] Z. Wang, S.R. Xu, Q.X. Sui, J. Wang, B. Liu, H. Wen, T.Y. Xiao, Q. Yuan, F.J. Zhao, J. Liu, High-performance martensitic stainless steel nanocomposite powder for direct energy deposition prepared by ball milling, Rare Met. 42 (2023) 2419–2432.
[16] C.L. Zhong, A. Gasser, J. Kittel, K. Wissenbach, R. Poprawe, Improvement of material performance of Inconel 718 formed by high deposition-rate laser metal deposition, Mater. Des. 98 (2016) 128–134.
[17] H.Z. Zhong, X.Y. Zhang, S.X. Wang, J.F. Gu, Examination of the twinning activity in additively manufactured Ti-6Al-4V, Mater. Des. 144 (2018) 14–24.
[18] F. Weng, Y.X. Chew, Z.G. Zhu, X.L. Yao, L.L. Wang, F.L. Ng, S.B. Liu, G.J. Bi, Excellent combination of strength and ductility of CoCrNi medium entropy alloy fabricated by laser aided additive manufacturing, Addit. Manuf. 34 (2020), 101202.
[19] Y.S. Kim, H. Chae, W. Woo, D.K. Kim, D.H. Lee, S. Harjo, T. Kawasaki, S.Y. Lee, Multiple deformation scheme in direct energy deposited CoCrNi medium entropy alloy at 210K, Mater. Sci. Eng. A 828 (2021), 142059.
[20] P.S. Xue, L.D. Zhu, J.S. Ning, Y. Ren, Z.C. Yang, S.H. Wang, P.H. Xu, G.R. Meng, Z. Liu, B. Xin, Effect of laser incident energy on the densification and structure–property relationships of additively manufactured CrCoNi medium-entropy alloy, Virtual. Phys. Prototyp. 16 (4) (2021) 404–416.
[21] X.H. Zhan, C.Q. Qi, J.J. Zhou, L.J. Liu, D.D. Gu, Effect of heat input on the subgrains of laser melting deposited Invar alloy, Opt. Laser Technol. 109 (2019) 577–583.
[22] J.D. Hunt, Steady State Columnar and Equiaxed Growth of Dendrites and Eutectic, Mater. Sci. Eng. 65 (1984) 75–83.
[23] E. Heyn, Reports of the technische hochschule zu Charlottenburg, Metallographist 6 (1903) 54–63.
[24] H.G. Li, Y.J. Huang, S.S. Jiang, Y.Z. Lu, X.Y. Gao, X.F. Lu, Z.L. Ning, J.F. Sun, Columnar to equiaxed transition in additively manufactured CoCrFeMnNi high entropy alloy, Mater. Des. 197 (2021), 109262.
[25] H.S. Tran, J. Tchuindjang, H. Paydas, A. Mertens, R.T. Jardin, L. Duchêne, R. Carrus, J. Lecomte-Beckers, A.M. Habraken, 3D thermal finite element analysis of laser cladding processed Ti-6Al-4V part with microstructural correlations, Mater. Des. 128 (2017) 130–142.
[26] H.G. Li, Y.J. Huang, J.F. Sun, Y.Z. Lu, The relationship between thermo-mechanical history, microstructure and mechanical properties in additively manufactured CoCrFeMnNi high entropy alloy, J. Mater. Sci. Technol. 77 (2021) 187–195.
[27] M. Gäumann, C. Bezençon, P. Canalis, W. Kurz, Single-crystal laser deposition of superalloys: processing–microstructure maps, Acta Mater. 49 (6) (2001) 1051–1062.
[28] X. Lin, Y.m. Li, M. Wang, L.P. Feng, J. Chen, W.D. Huang, Columnar to equiaxed transition during alloy solidification, Sci. China, Ser. E: Eng. Mater. Sci. 46 (5) (2003) 475–489.
[29] A.L. Greer, A.M. Bunn, A. Tronche, P.V. Evans, D.J. Bristow, Modelling of inoculation of metallic melts: application to grain refinement of aluminium by Al–Ti–B, Acta Mater. 48 (11) (2000) 2823–2835.
[30] V. Errico, A. Fusco, S.L. Campanelli, Effect of DED coating and DED + Laser scanning on surface performance of L-PBF stainless steel parts, Surf. Coat. Technol. 429 (2022), 127965.
[31] M.S. Pham, B. Dovgyy, P.A. Hooper, C.M. Gourlay, A. Piglione, The role of side-branching in microstructure development in laser powder-bed fusion, Nat. Commun. 11 (1) (2020) 749.
[32] Y.F. Wang, C.L. Zhang, C.F. Yu, L.L. Xing, K.L. Li, J.H. Chen, J. Ma, W. Liu, Z. J. Shen, Construction of Cellular Substructure in Laser Powder Bed Fusion, Metals 9 (11) (2019) 1231.
[33] W. Wei, Y.N. Zhou, W.B. Liu, N. Li, J.Z. Yan, H.P. Li, Microstructural Characterization, Mechanical Properties, and Corrosion Resistance of Dental Co-Cr-Mo-W Alloys Manufactured by Selective Laser Melting, J. Mater. Eng. Perform. 27 (10) (2018) 5312–5320.
[34] J. Fu, H. Li, X. Song, M.W. Fu, Multi-scale defects in powder-based additively manufactured metals and alloys, J. Mater. Sci. Technol. 122 (2022) 165–199.
[35] J. Zhang, Z.Y. Pang, L. Wang, C.C. Sun, N. Liu, H.M. Chen, Z.X. Cheng, K. Li, Microstructure and properties evolution of Al–17Si–2Fe alloys with addition of quasicrystal Al–Mn–Ti master alloy, Rare Met. 39 (2020) 1210–1221.
[36] X.T. Yang, X.Q. Li, Q.B. Yang, J.L. Duan, X.Y. Fu, H.L. Wei, W.S. Li, The microstructural evolution and wear properties of Ni60/high-aluminum bronze composite coatings with directional structure, Rare Met. 40 (2021) 952–960.
[37] A. Xue, X. Lin, L.L. Wang, X.F. Lu, L.K. Yuan, H.L. Ding, W.D. Huang, Achieving fully-equiaxed fine β-grains in titanium alloy produced by additive manufacturing, Mater. Res. Lett. 11 (1) (2022) 60–68.
[38] A.M. Mullis, R.F. Cochrane, Grain refinement and the stability of dendrites growing into undercooled pure metals and alloys, J. Appl. Phys. 82 (8) (1997) 3783–3790.
[39] A.M. Mullis, A model for spontaneous grain refinement in alloy systems at low undercooling, Mater. Sci. Eng. A 226–228 (1997) 804–808.
[40] D. Kashchiev, A. Borissova, R.B. Hammond, K.J. Roberts, Effect of cooling rate on the critical undercooling for crystallization, J. Cryst. Growth 312 (5) (2010) 698–704.
[41] B. Zhu, N. Leung, W. Kockelmann, S. Kabra, A.J. London, M. Gorley, M.J. Whiting, Y.Q. Wang, T. Sui, Revealing the residual stress distribution in laser welded Eurofer97 steel by neutron diffraction and Bragg edge imaging, J. Mater. Sci. Technol. 114 (2022) 249–260.
[42] M. Hakamada, Y. Nakamoto, H. Matsumoto, H. Iwasaki, Y.Q. Chen, H. Kusuda, M. Mabuchi, Relationship between hardness and grain size in electrodeposited copper films, Mater. Sci. Eng. A 457 (1) (2007) 120–126.
[43] M.Z. Hussain, J.T. Xiong, J.L. Li, F. Siddique, L.J. Zhang, X.R. Zhou, A study on strengthening and toughening mechanism of laser beam welded joint prepared between Ti–22Al–27Nb and Ti–6Al–4V with an interlayer of Nb, Mater. Sci. Eng. A 825 (2021), 141843.
[44] K. Sindo, Welding Metallurgy, (2nd Ed.), John Wiley & Sons, Ltd., 2002.
[45] X.R. Tan, G.P. Zhang, Q. Zhi, Z.X. Liu, Effects of milling on the microstructure and hardness of Al2NbTi3V2Zr high-entropy alloy, Mater. Des. 109 (2016) 27–36.
[46] J.B. Wang, X.L. Zhou, J.H. Li, J.L. Zhu, M.N. Zhang, A comparative study of Cu–15Ni–8Sn alloy prepared by L-DED and L-PBF: Microstructure and properties, Mater. Sci. Eng. A 840 (2022), 142934.
[47] Y. Wu, G. Liu, Z.Q. Liu, Z.J. Tang, B. Wang, Microstructure, mechanical properties and post-weld heat treatments of dissimilar laser-welded Ti2AlNb/Ti60 sheet, Rare Met. 42 (2023) 1332–1342.
[48] H. Gao, Y. Huang, W.D. Nix, J.W. Hutchinson, Mechanism-based strain gradient plasticity— I. Theory, J. Mech. Phys. Solids 47 (6) (1999) 1239–1263.
[49] L.P. Kubin, A. Mortensen, Geometrically necessary dislocations and strain-gradient plasticity: a few critical issues, Scr. Mater. 48 (2) (2003) 119–125.
[50] Y.L. Zhao, T. Yang, Y. Tong, J. Wang, J.H. Luan, Z.B. Jiao, D. Chen, Y. Yang, A. Hu, C.T. Liu, J.J. Kai, Heterogeneous precipitation behavior and stacking-fault-mediated deformation in a CoCrNi-based medium-entropy alloy, Acta Mater. 138 (2017) 72–82.
[51] R.X. Zhao, C.Y. Chen, S.S. Shuai, T. Hu, Y. Fautrelle, H.L. Liao, J. Lu, J. Wang, Z. M. Ren, Enhanced mechanical properties of Ti6Al4V alloy fabricated by laser additive manufacturing under static magnetic field, Mater. Res. Lett. 10 (8) (2022) 530–538.
[52] R. Wang, J. Wang, T.W. Cao, R.X. Zhao, X.F. Lu, W. Guan, T. Hu, S.S. Shuai, S. Z. Xu, W.D. Xuan, C. Panwisawas, C.Y. Chen, Z.M. Ren, Microstructure characteristics of a René N5 Ni-based single-crystal superalloy prepared by laser-directed energy deposition, Addit. Manuf. 61 (2023) 103363.